nature climate change

SUPPLEMENTARY INFORMATION

DOI: 10.1038/NCLIMATE1722

Management of trade-offs in geoengineering through optimal choice of non-uniform radiative forcing

Douglas G. MacMartin[1], David W. Keith[2], Ben Kravitz[3], and Ken Caldeira[3]

[1]Control and Dynamical Systems, California Institute of Technology
1200 E. California Blvd., Pasadena CA 91125
[2]School of Engineering and Applied Sciences and
Kennedy School of Government, Harvard University
[3]Department of Global Ecology, Carnegie Institution

The results in the paper assume linearity in order to simplify the optimization (see Methods). This is a reasonable assumption for this model, as illustrated in Figures S1–S3 and Table S1; this has also been shown to be sufficiently valid in previous studies [1, 2]. First, Figure S1 illustrates linearity of the zonal-mean and annual-mean temperature and precipitation responses due to solar (insolation) reduction (SR), for cases simulated at (a) different forcing amplitudes, but uniform in space and time, (b) different latitude distributions that sum to a uniform spatial forcing, and (c) different seasonal distributions that sum to a uniform temporal forcing. In all of these cases, linearity is a good approximation for the zonal-mean behavior. (Note for comparison, Fig. S4 shows the zonal-mean response to CO_2 forcing.) For the same cases as in Fig. S1, Table S1 gives a quantitative comparison of how well linearity predicts either global-rms or worst-case normalized temperature and precipitation changes used as optimization metrics; also shown is the prediction for Northern Hemisphere September sea-ice extent considered in Figure 3. The agreement is particularly striking for predicting the effect of a 1% uniform solar insolation reduction from the seasonally varying cases. Further averaging either in space (e.g., over Giorgi regions) or in time (e.g., considering annual rather than monthly changes) improves the predictions.

Figures S2 and S3 illustrate linearity by comparing the annual-mean precipitation predicted by the optimization (assuming linearity) to the response directly computed from a simulation that applied the optimized distribution of SR. Again, linearity is a good approximation, giving confidence in the qualitative conclusions based on the linearity assumption. The spatial and temporal distribution of forcing could in principle be further optimized using the GCM to evaluate the optimization metric; while this would account for nonlinearity, it would of course be computationally expensive.

Several additional optimization results beyond those presented in the paper are illustrated in Tables S2 and S3 and Figures S5 and S6. Table S2 and Figure S5 demonstrate that the conclusion that non-uniform SR can be used to significantly improve the residual temperature and precipitation changes for the worst-off region is robust to the choice of minimizing either monthly- or annual-average changes, and to the choice of minimizing at the grid-cell level of the model or spatially-averaged changes over Giorgi regions. Table S3 considers weighting based on area (as in the paper), population, or economic output, as in [2], while Fig. S6 plots the optimization results from Figure 3, considering the trade-off between minimizing only temperature residuals, only precipitation residuals, or a combination, but plots these as a function of the average insolation reduction required in order to more clearly show the quantitative decrease in SR required.

Tailoring the latitudinal and seasonal distribution of forcing allows significant reductions in the worst-case temperature or precipitation changes, but only a modest improvement in the global rms. The reason for this is that the distribution that best minimizes global rms temperature residuals increases the solar insolation reduction at the poles, while the distribution that best minimizes global rms precipitation residuals requires the opposite pattern (in this model). This is illustrated in Figures S7 and S8, which give the zonal and temporal dependence of forcing for both of these optimizations, expressed either as a percentage solar insolation reduction, or in $\mathrm{W\,m^{-2}}$, and the corresponding zonal-mean temperature and precipitation residuals.

Finally, the zonal and temporal dependence of both the forcing and the temperature and precipitation are shown for each of the 15 individual forcing patterns used here in Figures S9 to S13. The zonal response dependence is not shown in these two-dimensional plots; meridional and monthly dependence are shown as these are the only dependencies introduced in the forcing.

References

[1] Ban-Weiss, G. A., and K. Caldeira, "Geoengineering as an optimization problem," *Environ. Res. Lett.*, Vol. 5, 2010.

[2] Moreno-Cruz, J., K. Ricke, and D. W. Keith, "A simple model to account for regional inequalities in the effectiveness of solar radiation management," *Climatic Change*, Vol. 110, No. 3-4, 2011, pp. 649–668.

[3] Nordhaus, W., "Geography and macroeconomics: new data and new findings," *Proc. Natl Acad. Sci.*, Vol. 103, 2006, pp. 3510–3517.

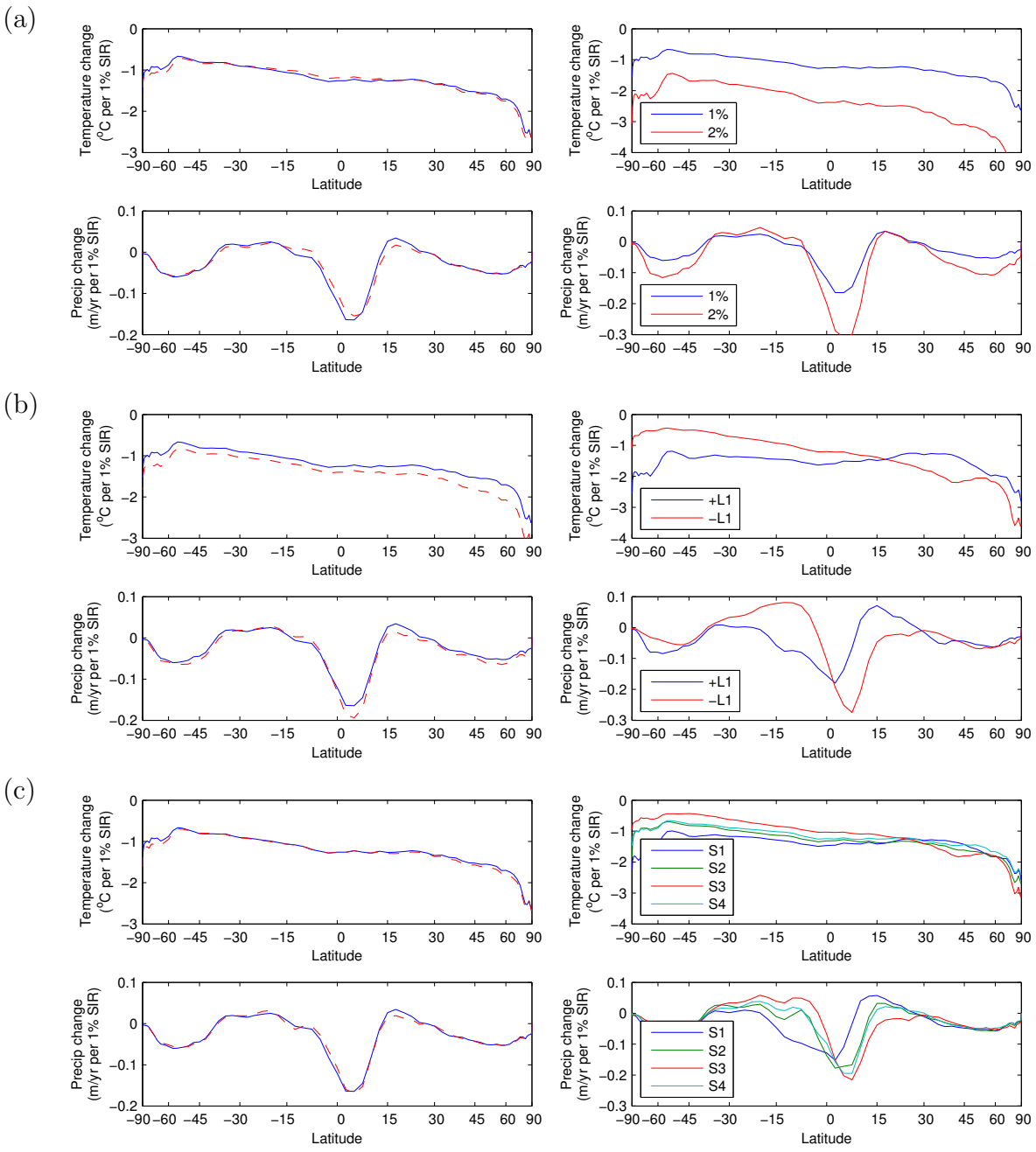

Figure S1: Linearity of model response to forcing: left-hand column compares the zonal-mean temperature and precipitation response due to a 1% solar reduction (SR) computed directly (blue) and the predicted response assuming linearity (red). The predicted responses are based on (a) a 2% constant uniform case to verify model linearity to forcing amplitude, (b) the sum of latitudinal dependence +L1 (constant plus linear increase with latitude) and −L1 forcing (constant plus linear decrease) to verify model linearity to combinations of patterns of spatial variation, and (c) the sum of spatially uniform but seasonally varying cases S1+S2+S3+S4 to verify model linearity to combinations of patterns of temporal variation (recall the temporal patterns sum to a constant). The right-hand column shows the response for each forcing distribution used in making the predictions.

1% SR metrics predicted from	Monthly, grid-cell rms	Monthly, grid-cell max	Annual, grid-cell rms	Annual, grid-cell max	Annual, Giorgi region rms	Annual, Giorgi region max	Sea ice ($\times 10^6$ km^2)
1% SR	3.03	22.7	2.90	16.4	2.56	14.8	2.95
2% SR	2.92	18.4	2.83	16.0	2.48	14.2	3.12
+L1 & −L1	3.42	25.0	3.30	18.4	2.93	16.7	3.56
S1, S2, S3 & S4	3.04	22.2	2.93	16.6	2.59	14.9	2.93

Table S1: Evaluation of linearity corresponding to the cases in Fig. S1: comparison of several of the climate metrics considered here computed directly from a uniform 1% SR, and the values predicted for 1% uniform SR assuming linearity and computed based on a different amplitude (2%), a combination of cases with spatially varying SR (+L1 & -L1), and a combination of cases with seasonally varying SR (S1–S4). Both the global-rms normalized temperature and precipitation changes and the worst-case over any region are evaluated, numbers given are the number of inter-annual standard deviations. Values of these metrics are shown at the grid-cell level for either monthly or annual-mean changes, and averaging over Giorgi regions; the linearity assumption improves with temporal and spatial averaging. The Northern Hemisphere September sea ice extent prediction is also shown in the final column (in millions of km^2); linearity is also a good approximation for this metric.

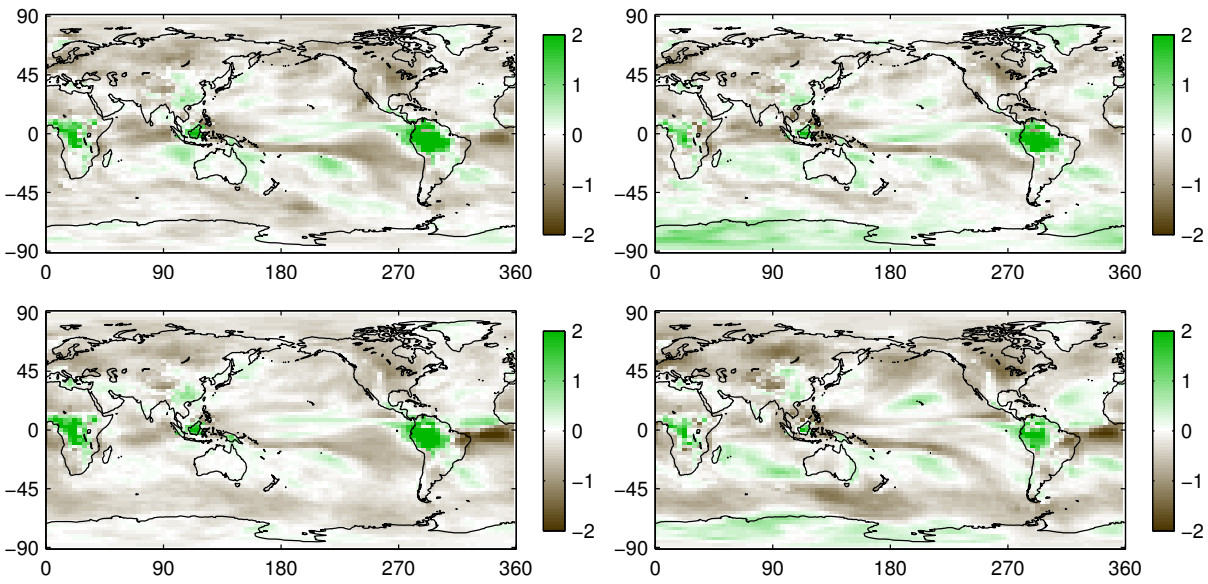

Figure S2: Direct verification of linearity, for an optimization minimizing global rms precipitation. The precipitation change relative to pre-industrial is shown in number of interannual standard deviations for uniform SR (left column), non-uniform optimum (right column), and predicted based on linear model (top row), or computed from direct simulation of the predicted optimal distribution (bottom row). Temperature changes (not shown) are in general more linear than precipitation changes.

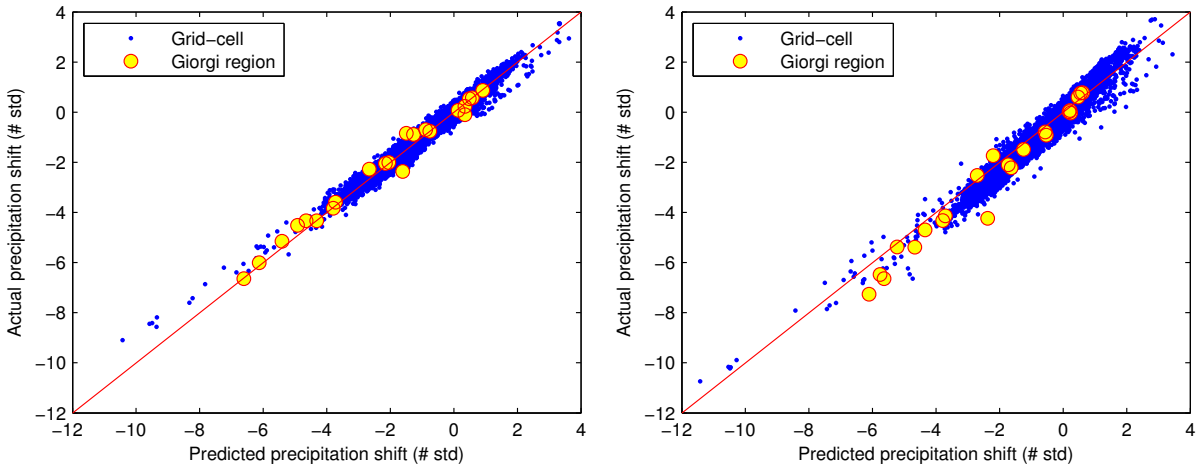

Figure S3: Direct verification of linearity, for same optimization cases as in Fig. S2. The precipitation change due to SRM is shown both at the grid-cell level and averaged over Giorgi regions for uniform SR (left) and non-uniform optimum (right).

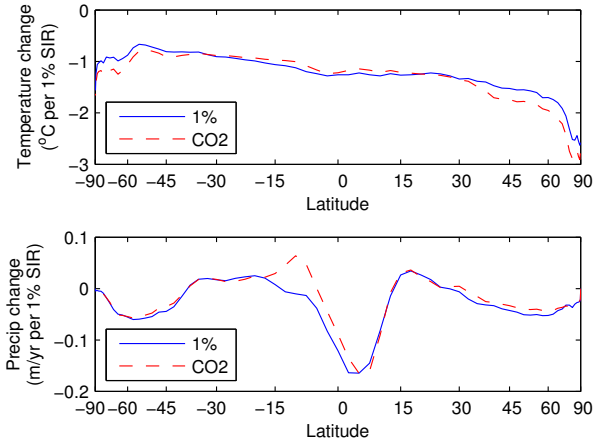

Figure S4: Zonal-mean temperature and precipitation response on same scale as Fig. S1, comparing the patterns of change due to CO_2 and due to solar insolation reduction. The latter is plotted for a 1% uniform reduction as in Fig. S1, and the former scaled and changed in sign for ease of comparison.

Spatial Scale	Time average	Optimization objective	rms residual			Worst-case residual		
			$2\times CO_2$	Uniform	N-dof	$2\times CO_2$	Uniform	N-dof
Grid-cell	Monthly	rms	7	**1.27**	**1.23**	28	13.5	14.8
		worst-case		3.7	2.3		**12.5**	**8.7**
	Annual	rms	6.7	**0.90**	**0.86**	19.7	4.8	4.8
		worst-case		1.37	1.28		**4.2**	**3.3**
Giorgi	Monthly	rms	6.6	**1.08**	**1.02**	21	5.3	5.5
		worst-case		1.1	1.2		**5.2**	**4.0**
	Annual	rms	6.5	**0.85**	**0.72**	18.8	3.6	2.7
		worst-case		1.3	0.85		**3.3**	**1.7**

Table S2: Normalized rms and worst-case temperature and precipitation residuals due to optimizing with either uniform (one degree of freedom) or the multiple degrees of freedom of spatial and temporal variation used here, and minimizing either the rms or the worst-case response. Both metrics are expressed in number of standard deviations; the entries corresponding to the optimization goal are shown in boldface. The first two rows of the table correspond to the optimizations shown with a '$\circ$' in Fig. 2 of the paper. The additional rows here illustrate the effect of considering only annual-mean rather than monthly-mean changes, and/or spatially-averaging over Giorgi regions rather than optimizing at the grid-cell level. The conclusion that significant reductions are achievable in the worst-case response is robust to both the choice of spatial scale and whether monthly or annual-mean response is optimized. Note that much of the reduction in worst-case can be achieved without significantly degrading the global rms residuals, as in Fig. 2; see Fig. S5.

	Uniform			N-dof		
	Area	Pop.	GDP	Area	Pop.	GDP
Area	**0.18**	0.21	0.22	**0.17**	0.21	0.20
Pop.	0.20	**0.20**	0.20	0.20	**0.17**	0.19
GDP	0.20	0.20	**0.20**	0.19	0.20	**0.17**

Table S3: Rms normalized temperature and precipitation response relative to the $2\times CO_2$ value (square root of quadratic impacts). Each column corresponds to evaluating the rms with a weighting on the changes in different grid cells either by grid-cell area, by population, or by GDP. Rows correspond to the optimization metric weighting the importance of each grid-cell based on area, population, or GDP; the value optimized in each row is thus along the diagonal, and shown in boldface. The difference in the optimal solution here for different weightings is small either with uniform SR (a single degree of freedom, left half), or spatial and temporal variation (multiple degree of freedom case, right half). Population and GDP data from [3].

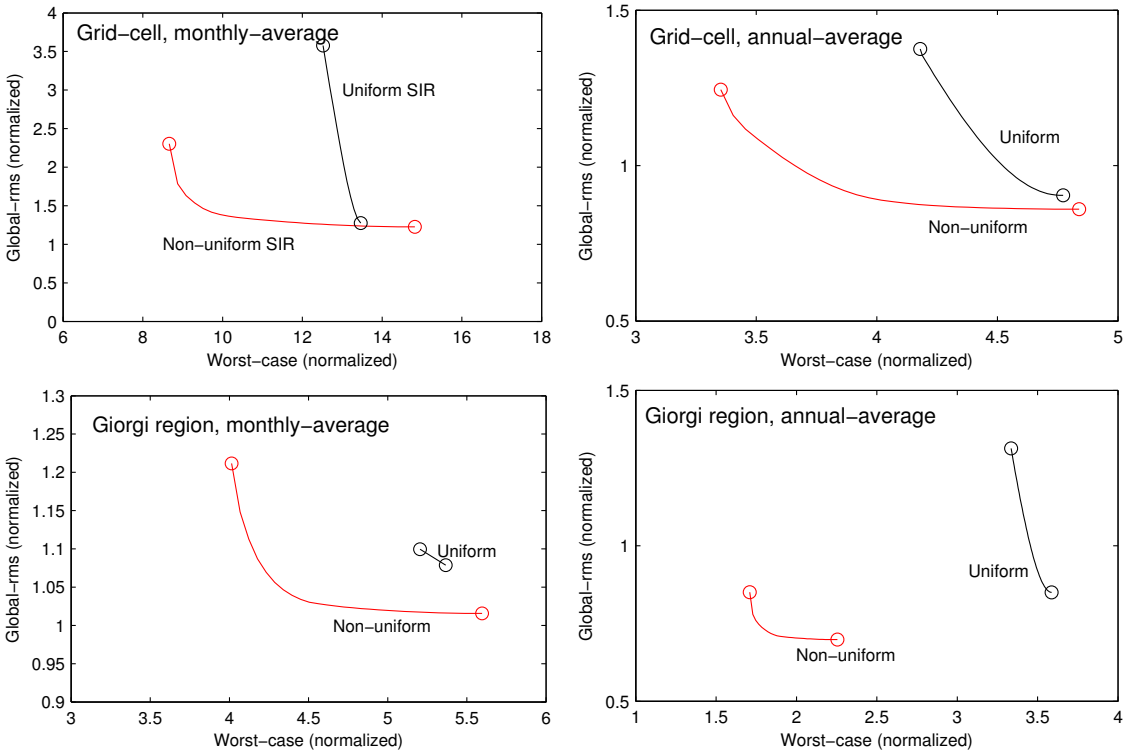

Figure S5: The trade-off between minimizing the global-rms normalized temperature and precipitation changes, and minimizing the worst-case change, optimizing either over grid-cells or Giorgi regions, and either monthly- or annual-average changes. The top-left (monthly-average grid-cell optimization) corresponds to Fig. 2 in the paper. In general, much of the reduction in worst-case residuals using non-uniform SR can be obtained without a significant increase in the global rms residuals.

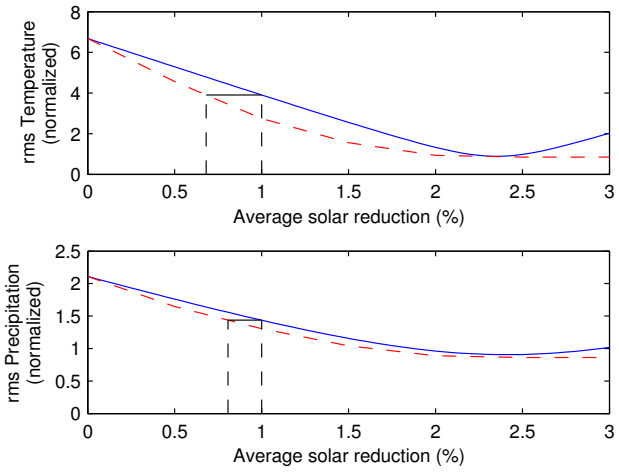

Figure S6: Normalized rms temperature (top) and precipitation (bottom) residuals for either uniform (solid line) or non-uniform (dashed, red) insolation reduction, plotted as a function of the average insolation reduction required. The non-uniform distribution is chosen to optimize only temperature or only precipitation residuals (same optimizations plotted in Fig. 3, lefthand panel). The average non-uniform SR required to obtain the same rms reductions as a 1% uniform SR is highlighted.

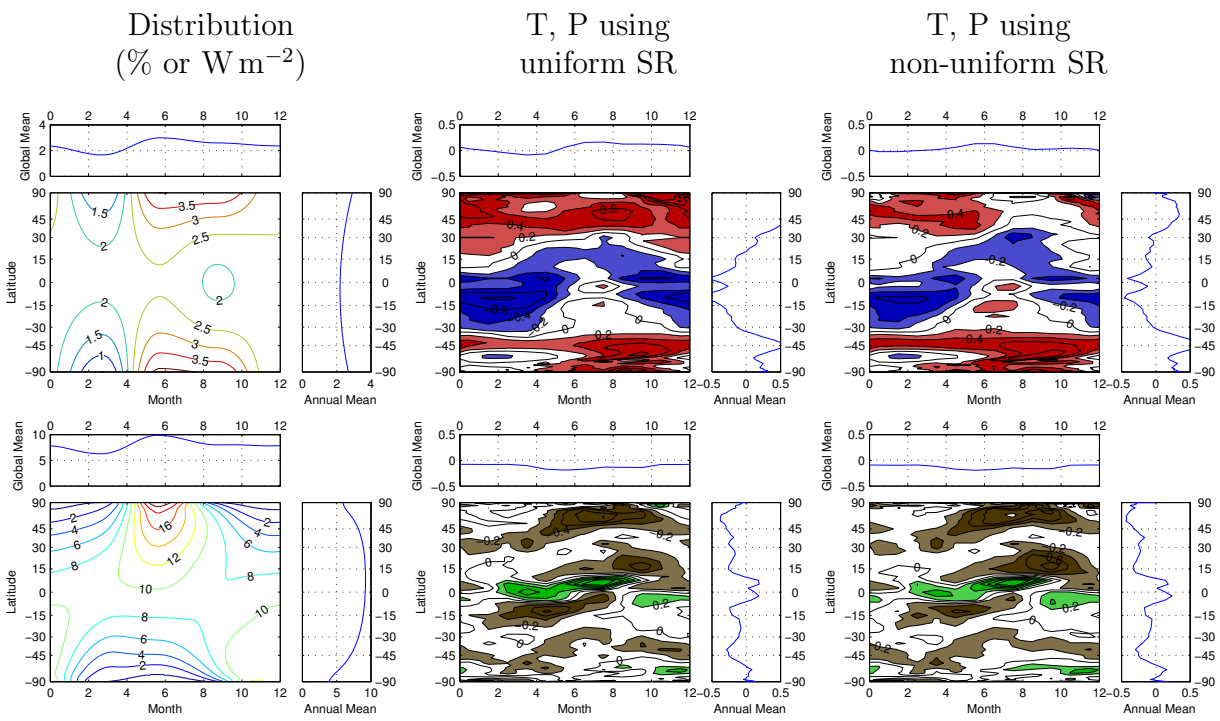

Figure S7: Latitudinal and temporal distribution of forcing that minimizes global rms temperature, and the resulting (predicted) zonal-mean response. The first column shows the optimal distribution of solar reduction expressed as percentage (top row) or W m^{-2} (bottom row). The next columns show the corresponding temperature residual (top row) or precipitation (bottom row) resulting from either the best uniform SR (middle column) or the optimized non-uniform distribution (final column). Temperature and precipitation are relative to baseline, and scaled by the standard deviation of interannual variability at each grid point. Contour intervals are 0.2 standard deviations, and shaded where the absolute value is larger than 0.2. Each of the six panels also includes the annual mean as a function of latitude and global mean as a function of time.

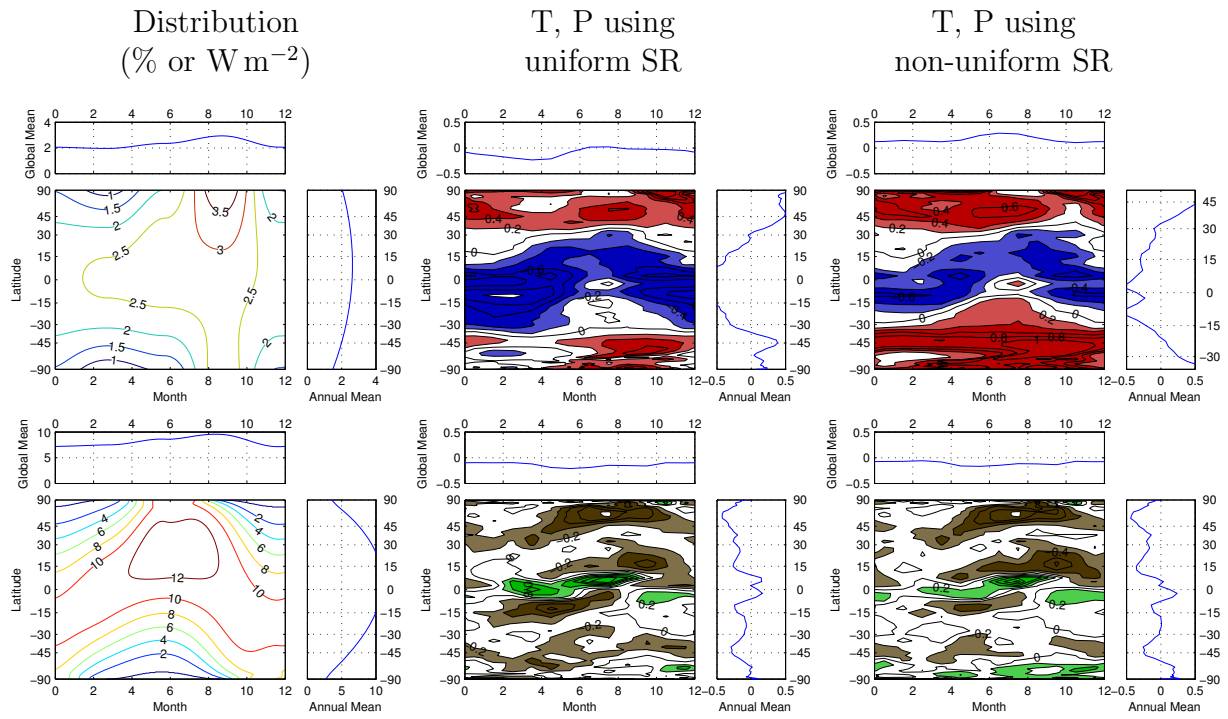

Figure S8: As Fig. S7, but for minimizing precipitation instead of temperature. Note that the distribution in Fig. S7 that minimizes temperature (greater emphasis on poles) is quite different from that which minimizes precipitation.

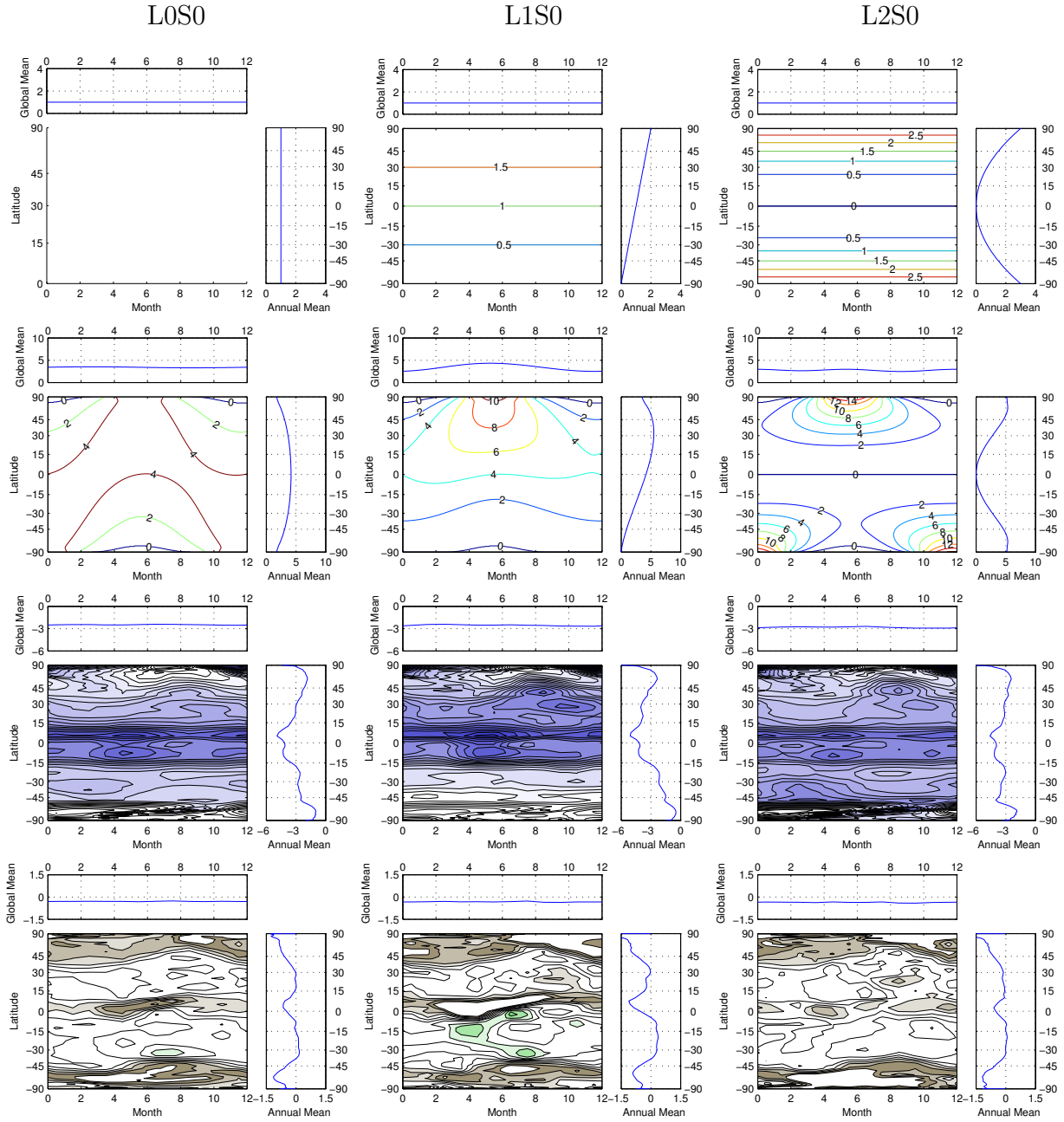

Figure S9: Latitudinal and temporal forcing and response for applied solar insolation reduction constant in time (S0) and varying spatially: uniform (L0), left column; linear (L1), middle column, and parabolic (L2), right column. Each distribution is normalized to give a spatially- and seasonally-averaged insolation reduction of 1%. Top row is the solar insolation reduction (%), second row the corresponding forcing in $\mathrm{W\,m^{-2}}$, and third and fourth rows the normalized temperature and precipitation change.

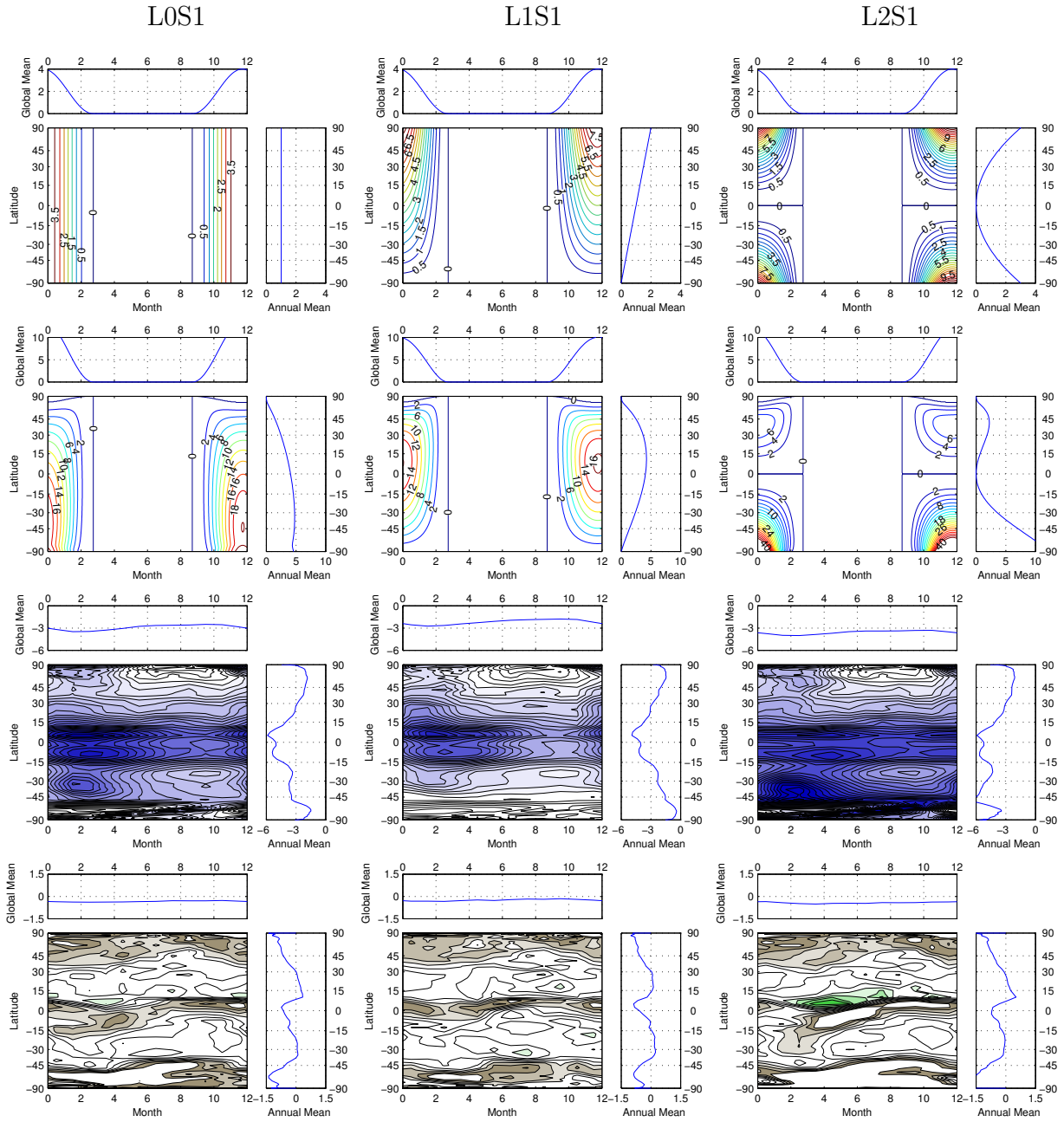

Figure S10: Latitudinal and temporal forcing and response for applied solar insolation reduction peaking in Northern Hemisphere winter (S1) and varying spatially: uniform (L0), left column; linear (L1), middle column, and parabolic (L2), right column. Each distribution is normalized to give a spatially- and seasonally-averaged insolation reduction of 1%. Top row is the solar insolation reduction (%), second row the corresponding forcing in $\mathrm{W\,m^{-2}}$, and third and fourth rows the normalized temperature and precipitation change.

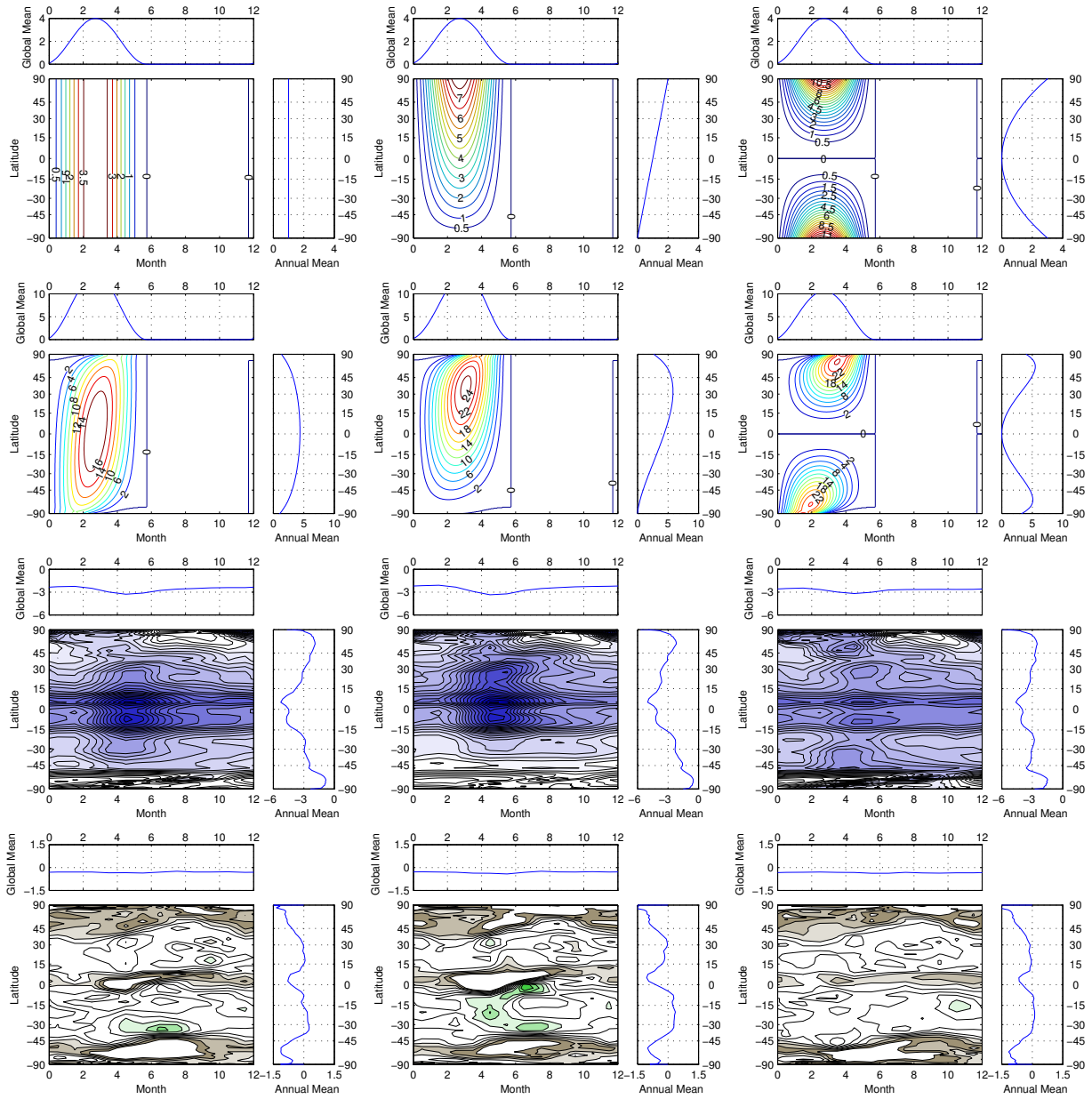

Figure S11: Latitudinal and temporal forcing and response for applied solar insolation reduction peaking in Northern Hemisphere spring (S2) and varying spatially: uniform (L0), left column; linear (L1), middle column, and parabolic (L2), right column. Each distribution is normalized to give a spatially- and seasonally-averaged insolation reduction of 1%. Top row is the solar insolation reduction (%), second row the corresponding forcing in $\mathrm{W\,m^{-2}}$, and third and fourth rows the normalized temperature and precipitation change.

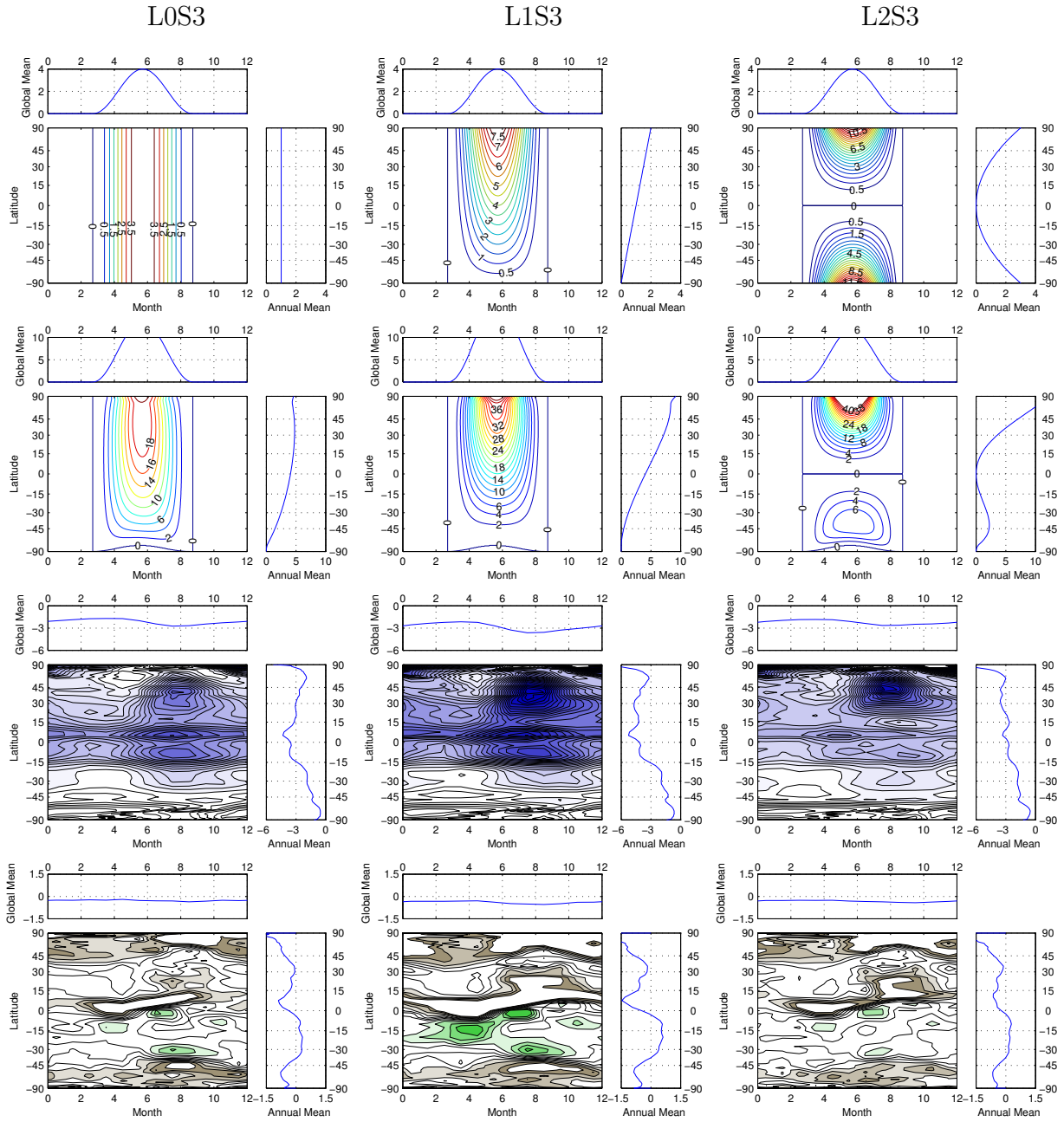

Figure S12: Latitudinal and temporal forcing and response for applied solar insolation reduction peaking in Northern Hemisphere summer (S3) and varying spatially: uniform (L0), left column; linear (L1), middle column, and parabolic (L2), right column. Each distribution is normalized to give a spatially- and seasonally-averaged insolation reduction of 1%. Top row is the solar insolation reduction (%), second row the corresponding forcing in $\mathrm{W\,m^{-2}}$, and third and fourth rows the normalized temperature and precipitation change.

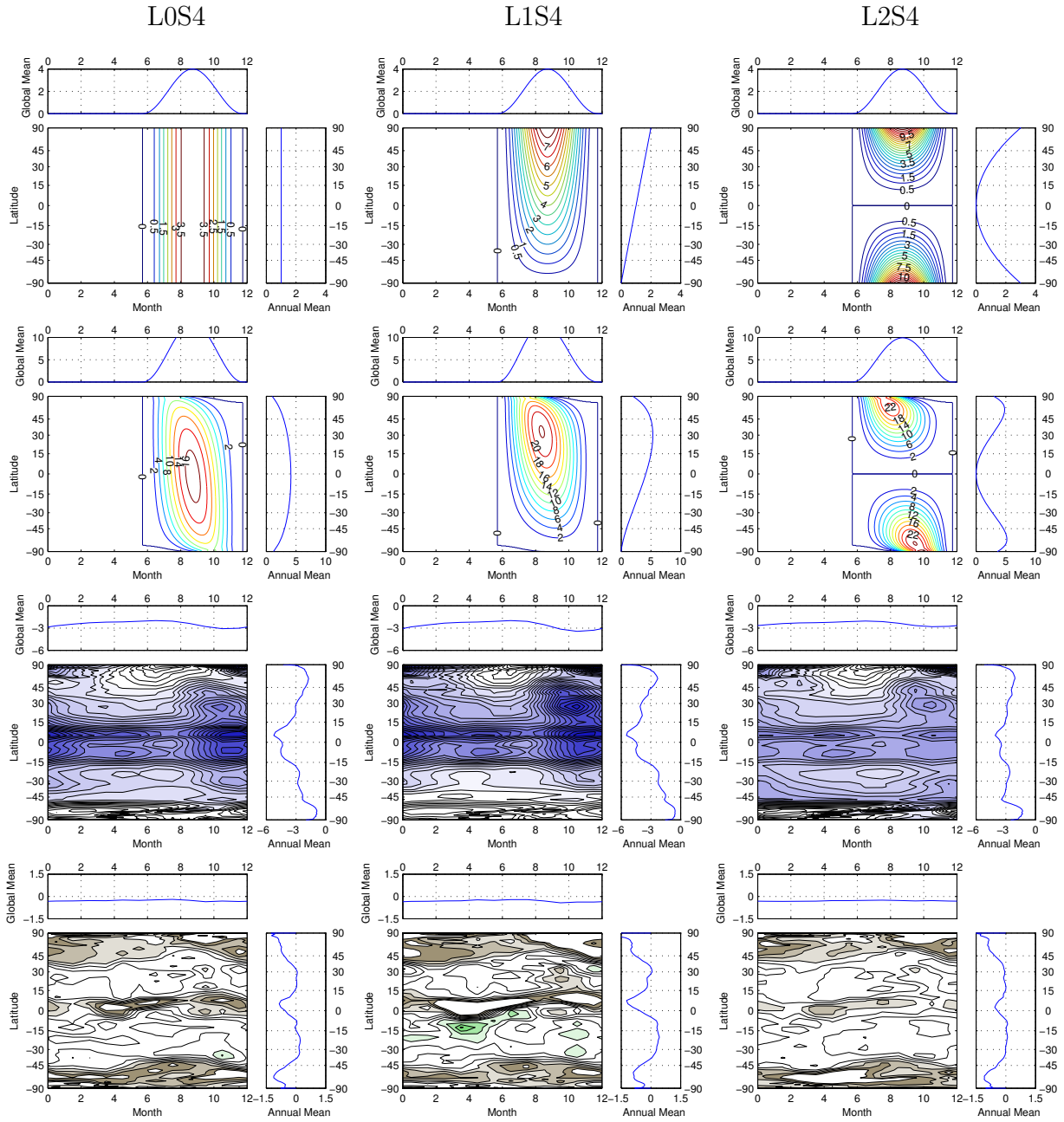

Figure S13: Latitudinal and temporal forcing and response for applied solar insolation reduction peaking in Northern Hemisphere autumn (S4) and varying spatially: uniform (L0), left column; linear (L1), middle column, and parabolic (L2), right column. Each distribution is normalized to give a spatially- and seasonally-averaged insolation reduction of 1%. Top row is the solar insolation reduction (%), second row the corresponding forcing in $\mathrm{W\,m^{-2}}$, and third and fourth rows the normalized temperature and precipitation change.